Stable and Catalytically Active Shape-Engineered Cerium Oxide Nanorods by Controlled Doping of Aluminum

Haoming Yan[a‡], Zhongqi Liu[b‡], Shize Yang[c‡], Xiaozhou Yu[a], Tao Liu[b], Qianying Guo[b,d], Junhao Li[b], Ruigang Wang[b*], and Qing Peng[a*]

[a]Department of Chemical and Biological Engineering, The University of Alabama, Tuscaloosa, AL 35487; [b]Department of Metallurgical and Materials Engineering, The University of Alabama, Tuscaloosa, AL 35487; [c]Materials Science and Technology Division, PO BOX 2008, Oak Ridge National Laboratory, Oak Ridge, TN 37831-6071; [d]Center for Nanophase Materials Sciences, PO BOX 2008, Oak Ridge National Laboratory, Oak Ridge, TN 37831-6071.

‡All authors contribute equally to this work.
*Corresponding Author: rwang@eng.ua.edu; qpeng2@eng.ua.edu

ABSTRACT

Shape-engineered nanocrystals (SENs) promise a better selectivity and a higher activity in catalytic reactions than the corresponding non-shape-engineered ones owing to their larger specific surface areas and desirable crystal facets. However, often, these SENs are less stable because the desirable surface facets have higher specific surface energies than other types of facets. Therefore, it is challenging to apply SENs in practical catalytic applications at high reaction temperatures to achieve favorable kinetics. In this paper, we show that atomic layer deposition of Al_2O_3 can modify the shape-engineered CeO_2 nanorods (NRs) to not only increase their shape transition temperature from 400 ºC to at least 700 ºC, but also greatly increase their specific reversible oxygen storage capacity (srOSC) up to 700 ºC. Through Al_2O_3 atomic layer deposition at 200 ºC, trimethyl aluminum reduces the Ce^{4+} to Ce^{3+} and substitutes Ce^{3+} ions with Al^{3+} to form -Al-O-Ce-O- structure. The substituted Al^{3+} ions impede the surface diffusion of Ce ions, therefore improve the thermal stability of CeO_2 NRs. The Ce ion in -Al-O-Ce-O-, a new Ce species, can be reversibly reduced and oxidized at 500 – 700 ºC. Our method presents a new strategy to improve the thermal stability and catalytic activities of SENs, thereby expand their applications into high temperature environments.

KEYWORDS: shape-engineered, ceria, aluminum oxide, atomic layer deposition, stability

INTRODUCTION

Cerium oxide (CeO_2) plays important roles as catalysts and/or catalyst supports in a wide range of applications, including three-way catalysts on catalytic converters of cars,[1] catalysts for fluidized-bed catalytic cracking,[2] catalytic oxidation of soot from diesel engines,[3] and solid oxide fuel cells,[4-5] to name a few. All of these applications utilize CeO_2 because it has an exceptionally large specific (per unit mass of CeO_2) reversible oxygen storage capacity (srOSC), which originates from the redox reactions: $2Ce_2O_3 + O_2 \rightleftarrows 4CeO_2$.[1] These practical applications demand not only a large srOSC but also a facile redox kinetics, *i.e.,* a large amount of srOSC that can be extracted at a lower temperature at a faster rate.[4, 6-15] The redox kinetics of pure CeO_2 depends strongly on its size, shape, and crystal facets.[12, 16-19] In comparison with other types of CeO_2 nanomaterials, shape-engineered CeO_2 nanorods (NRs) has more facile redox kinetics for srOSC,[12, 16, 18-19] owing to their unique physiochemical properties, including ***(i)*** the high density of {100} and {110} facets, which are more reducible than {111} facets;[12, 19-21] ***(ii)*** the high density of defects.[1, 12, 15, 22-24] However, these shape-engineered CeO_2 NRs permanently lose their facile redox kinetics if heated above 400 ºC, because they deform into thermally more stable octahedrons, which have {111} as the dominating surface facets, and aggregate.[15, 23, 25-27] This inferior thermal stability severely limits their applications in high temperature environments in order to achieve fast reaction kinetics.

The poor thermal stability of highly active SENs, including CeO_2 NRs, is due to the diffusion of surface and bulk atoms.[28-30] In order to diffuse, atoms need to break and reform bonds with surround atoms.[31] Diffusion of a surface atom is activated at lower temperatures than diffusion of a bulk atom because surface atoms have fewer bonds with the surrounding atoms than atoms in bulk. Therefore, it is possible to improve the thermal stability of SENs by suppressing the diffusion of surface atoms by surface modification.

In this paper, we present a new strategy that not only maintains the facile low temperature redox kinetics of srOSC of shape-engineered CeO_2 NRs, but also improves their thermal stability to at least 700 ºC so that a large amount of sub-surface and bulk oxygen can be extracted as well. Our method is to controllably modify these shape-engineered CeO_2 NRs with atomic layer deposition (ALD). Because the unique delayed nucleation of ALD Al_2O_3 on dehydrated CeO_2 NRs, Al dopes onto CeO_2 NRs and substituted some Ce ions on the surface of NRs on a large scale, while not fully cover the surface of NRs to deactivate their useful srOSC. The controlled Al dopants reduces the diffusion of surface atoms on CeO_2 by increasing the strength and number of chemical coordination of surface ions and by increasing the tortuosity and/or blocking the diffusion pathways of Ce ions of CeO_2.

RESULTS

Improved shape stability of shape-engineered CeO_2 NRs upto 700 ºC.

Figure 1 shows the low magnification TEM images of CeO_2 NRs followed by various treatments. Figure 1a shows a typical TEM image of shape-engineered CeO_2 NRs sample, which consists mainly of rods and the amount of other shapes is negligible. There is variation in the aspect ratios of CeO_2 NRs. These shape-engineered CeO_2 NRs were synthesized at temperatures lower than 100 ºC (details in the experimental section). As presented in Figure 1b, these CeO_2 NRs lose their rod shapes and transform into spherical or irregular-shaped nanoparticles after annealing at 700 ºC in air for 5h (this treatment is named as HT: high temperature treatment), suggesting that these CeO_2 NRs are thermally instable. The morphology change is consistent with literature observation of the CeO_2 NRs that are synthesized through the same method.[26-27] Figure 1c and 1d show that 45 cycles of Al_2O_3 ALD do not alter the rod morphology of CeO_2 NRs. Therefore, the ALD reaction temperature (200 ºC) and the ALD chemistry do not affect the morphology of the sample. For convenience, we name CeO_2 NRs after n cycles of Al_2O_3 ALD treatment as CeO_2NR/nAl_2O_3. Figure 1e and 1f show that $CeO_2NR/45Al_2O_3$ preserved its rod shape after annealed at 700 ºC in air for 5h. We name this sample as $CeO_2NRs/45Al_2O_3$_HT. In comparison with the results in Figure 1b, the results in Figure 1e-1f indicate that 45-cycle ALD Al_2O_3 treatment dramatically improves the thermal stability of the CeO_2 NRs. Figure 1g-1h present the morphology of the samples of $CeO_2NR/1Al_2O_3$_HT and $CeO_2NR/10Al_2O_3$_HT, which are named according to the same method as $CeO_2NR/45Al_2O_3$_HT. $CeO_2NR/1Al_2O_3$_HT has numerous spherical nanoparticles, while $CeO_2NR/10Al_2O_3$_HT has negligible spherical nanoparticles. Therefore, we conclude that ALD Al_2O_3 treatment can improve the morphology stability of shape-engineered CeO_2 NRs and the degree of stability enhancement depends on the number of ALD cycles.

High resolution scanning transmission electron microscopy (STEM) images were taken to understand the effect of Al_2O_3 ALD treatment on the detailed microstructure of CeO_2 NRs. Figure 2a and 2b show that CeO_2 NRs grow along the {110} direction with side surfaces of {100} and {110}. In addition, these CeO_2 NRs are well crystallized before ALD process. The figures show that these shape-engineered CeO_2 NRs have surface defects, which could contribute to the facile oxygen redox kinetics. As shown by Figure 2c and 2d, CeO_2NR/45Al_2O_3 still maintain {110} as the main axial and {100} and {110} as the surface facets along the sides of the CeO_2 NRs. We do not observe an amorphous Al_2O_3 shell around the CeO_2 NRs. This result is a surprise because 45 ALD cycles could produce amorphous Al_2O_3 shell of ~ 4-5 nm if Al_2O_3 ALD nucleation follows the typical steady state growth rate of Al_2O_3 ALD, which is around 1 Å/cycle at 200 ºC. Therefore, the nucleation of Al_2O_3 ALD is significantly delayed and we will discuss it in details in later sections.

The microstructures of CeO_2NR/45Al_2O_3_HT and CeO_2NR_HT were also analyzed by STEM to illustrate the effect of HT on the microscopic crystal structures of CeO_2 NRs. Figure S1a – S1c show some typical images from these analyses. According to the figures, the shape of nanorods is largely maintained for CeO_2NR/45Al_2O_3_HT sample. These nanorods have an average diameter less than 10 nm. Surfaces of these NRs become sharper than the CeO_2NR/45Al_2O_3. In contrast, CeO_2NR_HT sample mainly consists of large particles, as shown by Figure S1d. These large particles are generated from the deformation and aggregation of CeO_2 NRs owing to the thermal diffusion of Ce.[32-33] The main surface facet of these large nanoparticles is {111}, which is thermodynamically more stable than {110} and {100} facets but does not have low temperature oxygen storage capability.[12, 16-19] This shape transformation is consistent with the result in Figure 1b. Figure S1 confirms that the high temperature annealing does not affect the nanorod morphology of CeO_2NR/45Al_2O_3, while the same high temperature annealing transforms CeO_2 NRs into large CeO_2 nanoparticles with {111} surface facet.

The distribution of diameters of the shape-engineered CeO_2 NRs, CeO_2NR_HT CeO_2NR/45Al_2O_3, and CeO_2NR/45Al_2O_3_HT were measured and summarized in Figure 3. CeO_2NR/45Al_2O_3 and CeO_2NR/45Al_2O_3_HT have a similar average diameter as CeO_2 NRs. CeO_2NR_HT has a much larger diameter than the CeO_2 NRs and CeO_2NR/45Al_2O_3_HT. This result further confirmed that the ALD Al_2O_3 treatment can stabilize the morphology of CeO_2 NRs at high temperatures, i.e., 700 ºC in this study.

Improved reversible oxygen storage capacity of shape-engineered CeO_2 NRs

ALD Al_2O_3 can stabilize the shape of CeO_2 NRs, it is more important and interesting to find out how the ALD Al_2O_3 treatment affects the specific reversible oxygen storage capacity of the CeO_2 NRs. Figure 4 presents the H_2 consumption result (measured by hydrogen temperature programmed reduction, H_2-TPR, details in experimental section) as a function of temperature for the pure CeO_2 NRs and the CeO_2 NRs after various treatments. The integrated area below the curve represents the amount of H_2 consumption, *i. e.,* the amount of oxygen that can be extracted by H_2. As illustrated by the curve of 1st H_2-TPR cycle of CeO_2 NRs (Figure 4a), the reduction of fresh CeO_2 NRs by H_2 takes off around 260 ºC, peaks at 480 ºC, and ends at ~ 580 ºC. The second reduction peak takes off at 580 ºC and ascends to 700 ºC, which is the unbound temperature for the TPR experiment. The low temperature reduction peaked at 480 ºC is ascribed to the consumption of H_2 by surface oxygen on CeO_2 NRs. The reduction at higher temperature (>580 ºC) is due to the H_2 that reacts with the bulk oxygen inside of CeO_2 NRs. This H_2 consumption behavior matches well with literature results of the fresh CeO_2 NRs that are prepared in the similar way.[12, 18, 34] After cooling the sample down and leaving in air for a day at room temperature, we ran the 2nd cycle of H_2-TPR for the sample, whose reduction behavior differs dramatically from that in the 1st H_2-TPR cycle. Although the H_2 consumption still takes off at 260 ºC, the height of the 1st peak, which now shifts to 420 ºC, decreased dramatically. The 2nd reduction peak also decreased a lot. This reduction behavior is similar as that of CeO_2NR_HT

(Figure 4a), except that CeO_2NR_HT sample has a higher initial reduction temperature and much less H_2 consumption, *i.e.,* the specific quantity of reducible oxygen, because HT treatment deforms the shape-engineered CeO_2 NRs into spherical or irregular-shaped nanoparticles. According to these results, annealing fresh CeO_2 NR at 700 ºC in N_2 or H_2 will irreversibly damage the oxygen species that can be reduced at low temperatures. Figure 4a also illustrates how the number of ALD Al_2O_3 cycles affects the srOSC of CeO_2 NRs by comparing the TPR curves from CeO_2NRs/1Al_2O_3_HT, CeO_2NRs/10Al_2O_3_HT, and CeO_2NRs/45Al_2O_3_HT. CeO_2NRs/1Al_2O_3_HT shows a small H_2 consumption peak at ~480 ºC. CeO_2NRs/10Al_2O_3_HT has two H_2 consumption peaks at 420 ºC and 550 ºC and has a much larger amount of reducible oxygen than CeO_2NRs/1Al_2O_3_HT. In a similar fashion as CeO_2NRs/45Al_2O_3_HT, the peak of CeO_2NRs/10Al_2O_3_HT at 550 ºC is from a large amount of new types of oxygen species that can be reduced between 500 – 700 ºC. The CeO_2NRs/10Al_2O_3_HT has a smaller srOSC than CeO_2NRs/45Al_2O_3_HT in the temperature upto 700 ºC. In summary, Figure 4a show that ALD Al_2O_3 treatment increases the specific reversible OSC in CeO_2 NRs upto 700˚C and the degree of improvement increases with number of ALD cycles.

CeO_2NRs/45Al_2O_3_HT shows a dramatically different TPR behavior than CeO_2 NRs. *First,* the most significant feature is that CeO_2NRs/45Al_2O_3_HT maintained a stable H_2-TPR profile, *i.e.,* stable srOSC, as evidenced by the 1st-10th TPR cycles of the sample (Figure 4b). TPR up to 700 ºC did not damage its srOSC. The exposure to air at room temperature can quickly replenish oxygen back into the H_2-reduced CeO_2NRs/45Al_2O_3_HT. The 1st TPR cycle has a higher H_2 consumption peak at the low temperature reduction (~480 ºC) than that in 2-10 cycles of TPR is higher than that from the 1st cycle and the peak at 550 ºC improves as well, meaning that the 1st TPR cycle changed the material to a more stable form. *Second,* although CeO_2NRs/45Al_2O_3_HT has a smaller peak at ~450 ºC than that the 1st TPR cycle of the fresh CeO_2 NR, it consumes a much higher amount of H_2 at the temperature range of 450 - 600 ºC, according to the area

underneath the curve. This result suggests CeO_2NRs/45Al_2O_3_HT has a much larger srOSC than fresh CeO_2 NRs at temperature below 700 ºC. *Third,* CeO_2NRs/45Al_2O_3_HT has a much larger srOSC than CeO_2NR_HT. According to these results, we conclude that CeO_2NR/45Al_2O_3_HT has a much larger srOSC than pristine CeO_2 NRs upto 700 ºC and has oxygen species that can be reduced by H_2 between 500 ºC and 600 ºC, which is beneficial for applications demanding intermediate temperature below 700 ºC, such as intermediate-temperature fuel cells.

Chemical composition of CeO_2 NRs with ALD Al_2O_3 treatment and/or HT treatment

As TEM analyses of CeO_2NRs/45Al_2O_3 cannot clearly differentiate Al_2O_3 coating from CeO_2 NRs, we analyzed the nanoscale chemical composition of nanorods by HAADF-EDX mapping for samples of CeO_2NRs/45Al_2O_3 and CeO_2NRs/45Al_2O_3_HT. Figure 5a and 5e show the morphology of CeO_2NRs/45Al_2O_3 and CeO_2NRs/45Al_2O_3_HT respectively, confirming that CeO_2 NRs maintained the rod structure after high temperature treatment. The EDX mapping show that O and Ce are homogeneously distributed throughout the bulk of the CeO_2 NRs in CeO_2NRs/45Al_2O_3 (Figure 5c and 5d) and CeO_2NRs/45Al_2O_3_HT (Figure 5g and 5h). In contrast, Al is located at the external surface of the CeO_2 NRs (Figure 5b and 5f). Al does exist on the top ~ 1 nm region which is much thinner than a 4 – 5 nm shell what would be expected for 45 cycles ALD Al_2O_3 on the metal-OH surface.[35-36] In addition, the presence of Al is not continuous and conformal. These results suggest a different reaction mechanism than that in the common Al_2O_3 ALD. Based on the comparison between Figure 5b and 5f, HT treatment did not drive significant diffusion of Al into the bulk of CeO_2 NRs. It makes sense as Al-O bonds are stable at 700 ˚C. According to the overall EDX mapping of the CeO_2NRs/45Al_2O_3, Al distributes on all nanorods (Figure S2).

As ALD Al_2O_3 growth on CeO_2NRs at 200 ˚C does not follow the common nucleation and growth scheme on -OH surface, a different reaction mechanism happens. It was reported that –OH species on CeO_2 can be almost completely removed at 200 ˚C, which is same as our ALD

treatment temperature.[37-38] Therefore, we hypothesize that –OHs on these CeO_2 NRs were removed before the ALD Al_2O_3 treatment. To test our hypothesis, the same ALD sequence was applied onto the CeO_2 NRs at two different temperatures: 75˚C and 200˚C using the flat boat method (see in the experiment section). Figure 6 shows the TEM results of the CeO_2NRs/45Al_2O_3 and CeO_2NRs/45Al_2O_3(75C). At 200 ˚C, no visible Al_2O_3 shell was formed on the CeO_2NRs after 45 cycles of Al_2O_3 ALD (Figure 6a). At 75˚C, in contrast, an Al_2O_3 shell of ~4.5 nm thickness was formed over the CeO_2 NRs (Figure 6b). This result aligns with hypothesis. At 75 ˚C, the surface of CeO_2 NR is populated with –OHs, which promote the nucleation and growth the Al_2O_3 shell through the common binary Al_2O_3 ALD chemistry. At 200 ˚C, however, because –OH groups on CeO_2 surface were removed, TMA directly reacts with CeO_2 through a reaction mechanism that is different and slower than that of binary Al_2O_3 ALD chemistry. We will discuss it further in the discussion section.

Figure 7a and 7b show the deconvoluted Ce 3d XPS spectrum of CeO_2NRs and CeO_2NRs/45Al_2O_3, respectively. Ce 3d shows split peaks resulting from the different valence states of Ce, including Ce^{3+} and Ce^{4+}.[39-44] The Ce^{4+} $3d_{3/2}$ and Ce^{4+} $3d_{5/2}$ peaks are located at 916.9 eV and 899.1 eV ± 0.2 eV, respectively. The Ce^{3+} $3d_{3/2}$ and Ce^{3+} $3d_{5/2}$ peaks are located at 901.7 eV and 886.7 eV ± 0.2 eV, respectively.[39-44] Other small satellite peaks are due to the energy-gain processes, so-called shake-down peaks.[40, 45] The atomic concentration of Ce^{3+} increases from 0.266 (CeO_2NRs) to 0.298 (CeO_2NRs/45Al_2O_3) based on the quantification of the Ce 3d XPS peaks for the corresponding samples. The higher concentration of Ce^{3+} indicates that ALD Al_2O_3 treatment reduced CeO_2 NRs to generate O vacancies and/or mobile oxygen species on the CeO_2 NRs surface. It is likely that Al^{3+} substitutes Ce ions during the ALD treatment. In addition, according to the inset photos of these two samples, CeO_2NRs/45Al_2O_3 is darker than CeO_2NRs. The darker color is a sign of partial reduction of CeO_2.[46-47]

XRD spectra of CeO_2NRs and CeO_2NRs/45Al_2O_3 are presented in Figure 8. Both samples have the characteristic XRD peaks of CeO_2, including {111}, {200}, {220}, and {311}. These peaks

in CeO_2NRs/45Al_2O_3 shift to higher values of 2θ based on the comparison between two spectra. The calculated lattice constant of the non-treated CeO_2 NRs is 5.415 Å ± 0.0026 Å, which decreased to 5.408 Å ± 0.0019 Å after the ALD Al_2O_3 treatment. This suggests that Al ions substituted Ce ions to form Ce-Al-O_x lattices. The shift of 2θ aligns with metal ion substituted CeO_2.[48-49]

All of the ALD treatment for the samples used for the H_2-TPR activity test above were synthesized using the tubing method (details in the experiment section). We then tried the same treatment on the CeO_2 NRs synthesized using the flatboat method (details in the experiment section), and the TPR results of the flatboat method treated samples were very different with the tubing method treated samples, as shown in Figure 9. The difference between the tubing and the flatboat methods were mainly the CeO_2 NRs sample bed thickness. The powder bed thickness in the tubing method was ~3 mm and in the flatboat method was ~0.3 mm. The ratio of the sample bed thickness between the tubing method and the flatboat method was only around 10:1. The TPR results shows that when using the same ALD Al_2O_3 treatment sequence, the flatboat method treated CeO_2 NRs lost most of its surface srOSC before HT. The srOSC of the CeO_2NRs/45Al_2O_3_HT made by the flatboat method increased a little bit, which should be due to the change on the nanorod surface during the HT. Comparing to the CeO_2NRs/45Al_2O_3_HT made by the tubing method, the srOSC of the sample made by the flatboat method was much smaller. Therefore, the sample bed thickness must have affected the reaction. Based on the gas diffusion theory, it takes much longer time for TMA to diffuse through the thicker sample bed in the tubing method than the thinner sample bed in the flatboat method. Therefore, CeO_2 NRs have much less reaction time with TMA overall in the tubing method than in the flatboat method. According to the report of J. W. Elam, et, al,[50] the time for TMA to diffuse through the sample bed is proportional to the square of the sample bed thickness, so the time needed for TMA to diffuse through the sample bed is 100 times more in the tubing method. Because of this, the overall reaction time between the TMA, water and the CeO_2 NRs needed to be shorten when using flatboat method,

in order to have the similar average reaction time as the tubing method. To prove this hypothesis, another experiment was tried with only 1/10 of the TMA and water exposure time in each ALD cycle by using the flatboat method. The TPR result of the CeO_2NRs/45Al_2O_3_HT made by the flatboat method shows very similar result as the CeO_2NRs/45Al_2O_3_HT made by the tubing method, with a little bit lower surface reduction peak at ~480˚C and even better light-off temperature. This results indicate that the ALD Al_2O_3 on the CeO_2 NRs is a rate controlled reaction. Long reaction time can eliminate the srOSC of the CeO_2 NRs but short reaction time can enhance both the srOSC and the thermal stability of the CeO_2 NRs.

DISCUSSION

Based on the TEM (Figure 1) and TPR measurements (Figure 5), ALD Al_2O_3 treatment not only stabilizes the morphology of the CeO_2 NRs, but also increases their srOSC (up to 700 ˚C). This new type of CeO_2NRs/Al_2O_3 can be applied in applications that operate at the temperatures higher than 700 ˚C and require a high srOSC below 500 ˚C. In this section, we present our hypothetic mechanisms for the improved thermal stability of morphology and srOSC properties of CeO_2NRs/45Al_2O_3 and the formation mechanism of CeO_2NRs/45Al_2O_3.

Why does CeO_2NRs/45Al_2O_3 maintain the nanorod morphology up to 700 ˚C?

To answer this question, let's first exam why CeO_2 NRs deform into CeO_2 nanoparticles when they are annealed at temperatures higher than 400 ˚C (Figure 1). Note, similar deformation is observed by other researchers as well.[15, 23, 25-27] This deformation is driven by the minimization of the molar Gibbs energy of the material at the same temperature and pressure (1 atmospheric pressure). *First*, the deformation reduces the specific surface area, thereby the specific (per kg of CeO_2) surface Gibbs energy of the materials, because the resulting CeO_2 nanoparticles have a smaller specific surface area than the CeO_2 NRs. *Second*, the resulting CeO_2 nanoparticles have a lower surface energy per cm^2 than that of the original CeO_2 NRs because CeO_2 NRs is dominated with surface facets of {110} and {100}, which have higher surface energy than the dominating surface facets of {111} on CeO_2 nanoparticles.[12, 19-21] Therefore, thermodynamically, annealing reduces the specific surface area and surface energy per cm^2 of CeO_2 nanocrystals.

Kinetically, CeO_2 NRs deform into nanoparticles because Ce ion moves around faster at higher temperatures. At 400 ˚C or above, Ce ions on {110} and {100} surfaces acquire enough energy to break surface bonds and move around. Ce ions in the bulk of CeO_2 may move as well, but at a much slower rate, because atoms in bulk CeO_2 crystals form more bonds with surrounding atoms, and it takes a higher energy to break more bonds in order to move around. The migration of Ce ions is accelerated by increasing the temperature, therefore CeO_2 NRs deforms much faster at 700 ˚C than at 400 ˚C. Note, the migration of O ions does not cause the deformation of CeO_2

NRs. For example, during the reduction and oxidation of CeO_2 NRs, O ions diffuse easily in and out of CeO_2 without deforming the crystal lattice. The reversible oxygen diffusion plays a key role to produce the reversible oxygen storage capacity of CeO_2.[1, 51] Therefore, deformation of CeO_2 NRs is driven by the movement of Ce ions to reduce the material's Gibbs energy.

The thermally stable CeO_2NRs/45Al_2O_3 rods suggests that the migration of Ce ions is dramatically reduced in these samples in comparison with the pristine CeO_2 NRs. We hypothesize that the decorated Al_2O_3 nanoparticles play two roles in improving the shape stability of CeO_2 NRs. *First,* the decorated Al_2O_3 nanoparticles physically block and/or slow down the surface diffusion of Ce ions. It is known that the surface diffusion rates of atoms can be dramatically reduced by a step of one atomic height. *Second*, Al^{3+} will slow down the diffusion of Ce ions by substitute the Ce ions. Because Al-O bonding is strong and hard to break (evidenced by the absence of oxygen storage capacity of Al_2O_3), so the Al^{3+} ions block the Ce ions from moving around, therefore, the treated CeO_2 NRs became much more thermally stable.

Why does CeO_2NRs/45Al_2O_3 has a larger srOSC than CeO_2 NRs?

The following three mechanisms contribute to the improved srOSC of CeO_2NRs/45Al_2O_3 upto 700˚C. *First,* majority of reducible surface oxygen from Ce-O bonding are still available because Al_2O_3 ALD does not form a conformal coverage around CeO_2 due to the sluggish nucleation and growth kinetics of Al_2O_3 ALD on CeO_2 at 200 ˚C. This non-conformal coverage of Al_2O_3 is clearly evidenced by the HAADF-EDX analyses (Figure 5). The non-conformal coverage is also shown by the activated CeO_2NRs/45Al_2O_3 made by the flat boat method using the same ALD sequence as the tubing method (Figure 9). *Second,* new types of reducible Ce species emerge as shown by the new reduction signal range from 500 to 600 ˚C. Based on the experimental data and the literature reports, we hypothesized the higher srOSC is from the formation of reducible Al-O-Ce-O- species on the surface and the sub-surfaces of CeO_2 NRs.

Although oxygen in O-Al cannot move to create oxygen vacancy, oxygen that bonds to Ce in -Al-O-Ce-**O**- but is not shared with Al could be activated at a lower temperature than the

corresponding oxygen in bulk CeO_2 lattice. Such -Al-O-Ce-**O**- species can be formed by substituting Ce^{4+} (radius of 1.01 Å) with the smaller Al^{3+} ions (radius of 0.53 Å). In -Al-O-Ce-**O**-, the Al ion will bond to and draw the oxygen ions closer to Al. XRD spectra of CeO_2 NRs and $45Al_2O_3/CeO_2$NRs show that the lattice constant of CeO_2NRs/$45Al_2O_3$ is smaller than that of CeO_2 NRs. This fact is consistent with the formation of Al-O-Ce-O- structure,[48-49] because the lattice constant of CeO_2 is measured to be 5.415 Å, and the simulated lattice constant of Al-O-Ce-O- is ~3.772 Å.[52] In addition, DFT calculations from several reports show that the metal ion doped CeO_2 has longer Ce-O bond, which is weaker than the original bond.[43] The formation of Al-O-Ce-O- is consistent with findings in literature reports. For instance, literature reports that thermal stability of CeO_2 can be enhanced by doping with metal ions (M), such as La^{3+}, Zr^{4+}, Ti^{4+}, Sn^{4+} etc, [8, 49, 53-54] These small cation ions can substitute Ce^{4+} to form M-O-Ce-O- structure and the metal ion modified CeO_2 nanoparticles have better thermal stability and higher oxygen storage capacity.[8, 48-49, 53] Therefore, new Al-O-Ce-O_x species are formed in CeO_2NRs/$45Al_2O_3$ and can create more reducible oxygen species at 500 – 600 ˚C to generate higher srOSC.[48, 55-59] It is also interesting to note that these Al-O-Ce-O- sit in diversified environments, because oxygen reduction peak is wide, indicating the oxygen ions sit in different environments or different configurations.

How does ALD grow on CeO_2 NRs?

According to the TEM analysis, CeO_2NRs/$45Al_2O_3$ does not have a conformal 4-5 nm Al_2O_3-shell, which is expected for steady state 45 cycles of Al_2O_3 ALD on oxide surface covered by –OHs (Figure 6). The simplified reaction mechanism of TMA with -OH surface is shown in Eq. 1, where g represents gas, * represents the surface.

$$Al_2(CH_3)_6\ (g) + *\text{-}OH = *\text{-}O\text{-}Al\text{-}(CH_3)_2\text{-}Al(CH_3)_3 + CH_4\ (g) \qquad (1)$$

Our experiment results proved that Al_2O_3 ALD nucleates differently on –OH free CeO_2 NRs than on –OH dominated CeO_2 NRs at the growth temperature of 200 ˚C. Literature reported that almost all of the OH species are removed from CeO_2 at 200 ˚C.[37-38] Therefore, TMA directly reacts with Ce-O-Ce bond on the CeO_2 surface that is free of OH. TMA will compete with Ce for

oxygen because TMA is one of the strongest Lewis acids, meaning the Al atom can bond with a lone pair of electrons on O. This reaction will reduce Ce^{4+} to Ce^{3+} and create oxygen vacancies; Meanwhile, Al^{3+} cations from ALD Al_2O_3 will be incorporated into the lattice of CeO_2 NRs to form Al-O-Ce-O-on the surface, or even the subsurface of the NRs. XRD (Figure 8) confirms this incorporation of Al. The XPS analysis (Figure 7) shows that concentration of Ce^{3+} increases after the ALD Al_2O_3 treatment. -CH_3 ligands on TMA could be oxidized into carbonyl groups or CO_2. The reaction between TMA and CeO_2 produces a relatively inert surface so that the following cycles of ALD Al_2O_3 growth nucleates slowly.

There are methods to substitute Ce ions with other metal ions (M) to generate M-O-Ce-O-structure.[8, 43, 47-48] In these methods, precursors are mixed in solution and calcined at high temperatures. These methods generally produce doped CeO_2 samples of spherical particles with octahedral crystal structures. These doped CeO_2 particles do not have reducible oxygen at low temperatures, e. g, at 400 °C. Also high temperature annealing is required to activate these dopants in CeO_2 particles for reversible oxygen storage. It is not possible to use these previous methods to synthesize CeO_2 NRs and dope it with other metal ions due to its poor thermal stability and controlled synthesize conditions. Our method, here, presents a viable low temperature method to controllably doped CeO_2 NRs while enhances their low temperature rsOSC.

Also, based on the results from comparative experiments of the tubing method and the flatboat method, the ALD reaction with CeO_2 NRs has slow reaction rate. According to the TPR results in figure 9, long precursor exposure time in flatboat method can deactivate the CeO_2 NRs, but short exposure time can maintain or even enhance the OSC of CeO_2 NRs. This means TMA can slowly react with CeO_2 and turning the surface into $CeAlO_3$. If the reaction time is long enough, the whole surface will be turned into $CeAlO_3$ which completely blocked the O diffusion on the surface, so the TPR shows very small surface reduction peak at around 300-600˚C in Figure 9. If the reaction time is short, the surface is partially turned into the $CeAlO_3$, which create more reducible oxygen species on the surface and sub-surfaces which increased the srOSC of the NRs, so the TPR

shows very similar peaks as sample made by the tubing method (Figure 9). It is noticeable that the surface reduction peak around 450-500˚C of the 1/10 precursors exposure time using flatboat method in is smaller than the surface peak of CeO_2NRs/45Al_2O_3 using tubing method. The reason could be that even 1/10 of the precursors exposure time is too long, so there are too much $CeAlO_3$ generated on the CeO_2 NR surface, which decreased the amount of the reducible oxygen species on the surface.

CONCLUSIONS

We presented a viable and controllable Al doping method, *i. e.,* ALD Al_2O_3 at 200 ˚C, to improve the thermal stability of CeO_2 NRs as well as their srOSC. This method is novel as it not only sustains the morphology of CeO_2 NRs at high temperature but also enhance its thermal stability and rsOSC. Although shape-engineered nanocrystals (SENs) have the applications in a range of fields, including catalysis, photonics, optoelectronics, surface enhanced Raman scattering, and environmental issue, they often suffer from the poorer stability. Our method and the concept underlying this method could be adopted to improve thermal stability of other SENs while maintain or even enhance their unique functionalities.

METHODS

Preparation of CeO_2 nanorods.

The CeO_2 nanorods were synthesized through a hydrothermal method. Briefly, 8mL of 6 M NaOH aqueous solution were added into 0.1 M $Ce(NO_3)_3 \cdot 6H_2O$ (Acros Organics 99.5%). This mixture was stirred for about 15 s in a Teflon bottle (200 mL). The Teflon-lined autoclave was then tightly sealed and transferred into a programmable box furnace. The hydrothermal reaction procedure was carried out at 90 °C (CeO_2-NR) for 48 hrs. After the autoclave was cooled down to room temperature, the precipitates were collected, and then washed with deionized water and ethanol. The as-prepared samples were obtained by drying in air at 60 °C overnight.

ALD Chemical and materials

ALD precursors are trimethyl aluminum (TMA) (98%, Strem Chemicals) and deionized water (DI H_2O) (18 MΩ, water filtration system from Thermo Fisher Scientific LLC). The carrier and purging gas for the ALD process is ultrahigh purity N_2 (99.999%, Airgas). Isopropyl alcohol (IPA) (99.5% BDH) was used to clean the sample holder. HNO_3 (68-70%, BDH) and H_2O_2 (30%, BDH) were used for the ICP measurement.

ALD sample holder cleaning

Sample holders used in the ALD process include ceramic boat and quartz tube are cleaned by 30 min sonication (Branson 5510) in DI water and IPA, respectively, and dried on the hotplate at 400 °C for 1 hour. The metal wire cloth (Gerard Daniel Worldwide) covered on the ceramic boat is cleaned by the same procedure.

ALD processes

Tubing method

A quartz tube with diameter of 10 mm was used as the ALD sample holder for CeO_2 nanorods. CeO_2 nanorods are loaded into the quartz tube with one side blocked by the quartz wool, another

side of the tube is also blocked by the quartz after the sample loading. The average CeO_2 nanorod bed thickness in the quartz tube is 3 mm. The precursors for the Al_2O_3 ALD are TMA and DI H_2O. Due to the difficulty of the gas diffusion into the closed packed nanorod sample bed, long exposure time was used for the precursors. The temperature of the ALD chamber is 200 °C. The ALD sequence is: pre-purge the sample for 20 mins; pumping down the system to 10^{-2} torr; shut down the pump; TMA pulsing for 8 s (~ 2 torr); TMA exposure for 5 min; pump out TMA until system is 10^{-2} torr; N_2 purging for 120 s; H_2O dose for 20 s with carrier gas flow; N_2 purging for 120 s. Repeat the sequence for another layer of coating. The chamber is continuously vibrating by a homemade vibrator during the ALD process.

Flat-boat method

A ceramic boat with flat bottom was used as the ALD sample holder for CeO_2 nanorods. Nanorods are loaded into the boat and shook into a thin film which uniformly cover the bottom of the boat. The film thickness is ~ 0.3 mm. The precursors for the Al_2O_3 ALD are TMA and DI H_2O.

1. Normal flat-boat ALD coating

The temperature of the ALD chamber is 200 °C. The ALD sequence is: pre-purge the sample for 20 mins; pumping down the system to 10^{-2} torr; shut down the pump; TMA pulsing for 8 s (~ 2 torr); TMA exposure for 5 min; pump out TMA until system is 10^{-2} torr; N_2 purging for 120 s; H_2O dose for 20 s with carrier gas flow; N_2 purging for 120 s. Repeat the sequence for another layer of coating.

2. Low temperature flat-boat ALD coating

To verify if the rate limiting step in this ALD coating process is the reaction speed, the ALD chamber temperature was set to 136 °C. Based on the Arrhenius Equation, the reaction speed at 136 °C should be around 1/10 of the reaction speed at 200 °C. Other ALD sequences are kept the same as the normal flat-boat ALD coating method.

3. 1/10 exposure time flat-boat ALD coating

To verify if the rate limiting step in this ALD coating process is the diffusion speed, the exposure time of the precursors are decreased into 1/10 of the normal exposure time. Therefore, the TMA exposure time is 30 s and the H_2O dose is 2 s. All the other experiment conditions and ALD sequences are kept the same as normal flat-boat ALD coating method.

Heat treatment

Samples were loaded into a quartz boat and annealed inside the heat furnace (Lindberg/Blue M, ThermoFisher) at 700 °C for 5 hours in air. The ramping rate of the temperature is 10 °C/min.

Characterizations

TEM

TEM (FEI Tecnai F-20) was used to verify the morphology change of the CeO_2 nanorods before and after the heat treatment. The nanorod powder sample was dispersed into the methanol by sonication and the solution was drop casted onto the copper TEM grid (Supported carbon film, 200 mesh, TED PELLA).

STEM

Electron microscopy was carried out using Hitachi HF3300 high-resolution TEM-STEM at 300 kV and Nion UltraSTEM 200 at 200 kV. EDX mapping was carried out using FEI Talos microscope at 200 kV.

TPR

Hydrogen temperature programmed reduction (H_2-TPR) was performed using a Micrometrics AutoChem™ II 2920 with the temperature rising from ambient temperature to 700 °C at a rate of 10 °C/min. The gas mixture of 5% H_2 and 95% Ar passed through the different samples (~100 mg or normalized after ALD) loaded in a quartz U-type reactor with flowing rate of 50 mL/min.

H_2-TPR cycling experiment were performed 10 times in the same experimental apparatus with temperature also rising from ambient temperature to 700 °C. Between each H_2-TPR cycle, the quartz U-type reactor was taken down from the instrument and exposed in air for 24 hrs.

Acknowledgement

PENG thanks the Donors of the American Chemical Society Petroleum Research Fund for supporting this research. WANG thanks the financial support from the National Science Foundation (NSF CHE-1657943). Electron microscopy at ORNL (S.Z.Y.) was supported by the U.S. Department of Energy, Office of Science, Basic Energy Sciences, Materials Sciences and Engineering Division and performed in part as a user proposal at the ORNL Center for Nanophase Materials Sciences, which is a DOE Office of the Science User Facilities. This research used resources of the Center for Functional Nanomaterials, which is a U.S. DOE Office of Science Facility, at Brookhaven National Laboratory under Contract No. DE-SC0012704.

REFERENCES AND NOTES

1. Montini, T.; Melchionna, M.; Monai, M.; Fornasiero, P., Fundamentals and Catalytic Applications of CeO2-Based Materials. *Chem Rev* **2016,** *116* (10), 5987-6041.
2. Vogt, E. T. C.; Weckhuysen, B. M., Fluid catalytic cracking: recent developments on the grand old lady of zeolite catalysis. *Chemical Society Reviews* **2015,** *44* (20), 7342-7370.
3. Fino, D.; Bensaid, S.; Piumetti, M.; Russo, N., A Review on the Catalytic Combustion of Soot in Diesel Particulate Filters for Automotive Applications: From Powder Catalysts to Structured Reactors. *Applied Catalysis A-General* **2016,** *509*, 75-96.
4. Murray, E. P.; Tsai, T.; Barnett, S. A., A Direct-Methane Fuel Cell with a Ceria-Based Anode. *Nature* **1999,** *400* (6745), 649-651.
5. Desaunay, T.; Bonura, G.; Chiodo, V.; Freni, S.; Couzinie, J. P.; Bourgon, J.; Ringuede, A.; Labat, F.; Adamo, C.; Cassir, M., Surface-dependent oxidation of H-2 on CeO2 surfaces. *J. Catal.* **2013,** *297*, 193-201.
6. Yao, H. C.; Yao, Y. F. Y., Ceria in Automotive Exhaust Catalysts .1. Oxygen Storage. *J. Catal.* **1984,** *86* (2), 254-265.
7. Shyu, J. Z.; Weber, W. H.; Gandhi, H. S., Surface Characterization of Alumina-Supported Ceria. *J. Phys. Chem.* **1988,** *92* (17), 4964-4970.
8. Fornasiero, P.; Balducci, G.; DiMonte, R.; Kaspar, J.; Sergo, V.; Gubitosa, G.; Ferrero, A.; Graziani, M., Modification of the Redox Behaviour of CeO2 Induced by Structural Doping with ZrO2. *J. Catal.* **1996,** *164* (1), 173-183.
9. Vlaic, G.; Fornasiero, P.; Geremia, S.; Kaspar, J.; Graziani, M., Relationship between the Zirconia-Promoted Reduction in the RH-Loaded Ce0.5Zr0.5O2 Mixed Oxide and the Zr-O Local Structure. *J. Catal.* **1997,** *168* (2), 386-392.
10. Trovarelli, A.; de Leitenburg, C.; Boaro, M.; Dolcetti, G., The utilization of ceria in industrial catalysis. *Catal. Today* **1999,** *50* (2), 353-367.
11. He, J. J.; Wang, C. X.; Zheng, T. T.; Zhao, Y. K., Thermally Induced Deactivation and the Corresponding Strategies for Improving Durability in Automotive Three-Way Catalysts. *Johnson Matthey Tech* **2016,** *60* (3), 196-203.
12. Zhou, K. B.; Wang, X.; Sun, X. M.; Peng, Q.; Li, Y. D., Enhanced catalytic activity of ceria nanorods from well-defined reactive crystal planes. *J Catal* **2005,** *229* (1), 206-212.
13. Liu, X. W.; Zhou, K. B.; Wang, L.; Wang, B. Y.; Li, Y. D., Oxygen Vacancy Clusters Promoting Reducibility and Activity of Ceria Nanorods. *J. Am. Chem. Soc.* **2009,** *131* (9), 3140-3141.
14. Ta, N.; Liu, J. Y.; Chenna, S.; Crozier, P. A.; Li, Y.; Chen, A. L.; Shen, W. J., Stabilized Gold Nanoparticles on Ceria Nanorods by Strong Interfacial Anchoring. *J. Am. Chem. Soc.* **2012,** *134* (51), 20585-20588.
15. Wu, Z. L.; Li, M. J.; Howe, J.; Meyer, H. M.; Overbury, S. H., Probing Defect Sites on CeO2 Nanocrystals with Well-Defined Surface Planes by Raman Spectroscopy and O-2 Adsorption. *Langmuir* **2010,** *26* (21), 16595-16606.
16. Wu, Z. L.; Li, M. J.; Overbury, S. H., On the structure dependence of CO oxidation over CeO2 nanocrystals with well-defined surface planes. *J Catal* **2012,** *285* (1), 61-73.
17. Wu, Z. L.; Li, M. J.; Mullins, D. R.; Overbury, S. H., Probing the Surface Sites of CeO2 Nanocrystals with Well-Defined Surface Planes via Methanol Adsorption and Desorption. *Acs Catal* **2012,** *2* (11), 2224-2234.
18. Tong, X. F.; Luo, T.; Meng, X.; Wu, H.; Li, J. L.; Liu, X. J.; Ji, X. N.; Wang, J. Q.; Chen, C. S.; Zhan, Z. L., Shape-Dependent Activity of Ceria for Hydrogen Electro-Oxidation in Reduced-Temperature Solid Oxide Fuel Cells. *Small* **2015,** *11* (41), 5581-5588.
19. Mai, H. X.; Sun, L. D.; Zhang, Y. W.; Si, R.; Feng, W.; Zhang, H. P.; Liu, H. C.; Yan, C. H., Shape-selective synthesis and oxygen storage behavior of ceria nanopolyhedra, nanorods, and nanocubes. *J Phys Chem B* **2005,** *109* (51), 24380-24385.

20. Baudin, M.; Wojcik, M.; Hermansson, K., Dynamics, Structure and Energetics of the (111), (011) and (001) Surfaces of Ceria. *Surf. Sci.* **2000,** *468* (1-3), 51-61.
21. Nolan, M.; Grigoleit, S.; Sayle, D. C.; Parker, S. C.; Watson, G. W., Density functional theory studies of the structure and electronic structure of pure and defective low index surfaces of ceria. *Surf. Sci.* **2005,** *576* (1-3), 217-229.
22. Trovarelli, A.; Llorca, J., Ceria Catalysts at Nanoscale: How Do Crystal Shapes Shape Catalysis? *Acs Catalysis* **2017,** *7* (7), 4716-4735.
23. Aneggi, E.; Wiater, D.; de Leitenburg, C.; Llorca, J.; Trovarelli, A., Shape-Dependent Activity of Ceria in Soot Combustion. *Acs Catalysis* **2014,** *4* (1), 172-181.
24. Esch, F.; Fabris, S.; Zhou, L.; Montini, T.; Africh, C.; Fornasiero, P.; Comelli, G.; Rosei, R., Electron Localization Determines Defect Formation on Ceria Substrates. *Science* **2005,** *309* (5735), 752-755.
25. Jones, J.; Xiong, H. F.; Delariva, A. T.; Peterson, E. J.; Pham, H.; Challa, S. R.; Qi, G. S.; Oh, S.; Wiebenga, M. H.; Hernandez, X. I. P.; Wang, Y.; Datye, A. K., Thermally Stable Single-Atom Platinum-on-Ceria Catalysts via Atom Trapping. *Science* **2016,** *353* (6295), 150-154.
26. Zhu, S. H.; Lian, X. Y.; Fan, T. T.; Chen, Z.; Dong, Y. Y.; Weng, W. Z.; Yi, X. D.; Fang, W. P., Thermally stable core-shell Ni/nanorod-CeO2@SiO2 catalyst for partial oxidation of methane at high temperatures. *Nanoscale* **2018,** *10* (29), 14031-14038.
27. Mock, S. A.; Sharp, S. E.; Stoner, T. R.; Radetic, M. J.; Zell, E. T.; Wang, R., CeO2 nanorods-supported transition metal catalysts for CO oxidation. *Journal of colloid and interface science* **2016,** *466*, 261-267.
28. Forzatti, P.; Lietti, L., Catalyst deactivation. *Catal Today* **1999,** *52* (2-3), 165-181.
29. Zeng, P.; Zajac, S.; Clapp, P. C.; Rifkin, J. A., Nanoparticle sintering simulations. *Mat Sci Eng a-Struct* **1998,** *252* (2), 301-306.
30. Cao, A.; Lu, R.; Veser, G., Stabilizing metal nanoparticles for heterogeneous catalysis. *Phys Chem Chem Phys* **2010,** *12* (41), 13499-13510.
31. Shewmon, P., *Diffusion in solids*. Springer: 2016.
32. McCarty, J. G.; Gusman, M.; Lowe, D.; Hildenbrand, D.; Lau, K., Stability of supported metal and supported metal oxide combustion catalysts. *Catal Today* **1999,** *47* (1-4), 5-17.
33. Bartholomew, C. H., Mechanisms of catalyst deactivation. *Appl Catal a-Gen* **2001,** *212* (1-2), 17-60.
34. Lopez, J. M.; Gilbank, A. L.; Garcia, T.; Solsona, B.; Agouram, S.; Torrente-Murciano, L., The prevalence of surface oxygen vacancies over the mobility of bulk oxygen in nanostructured ceria for the total toluene oxidation. *Appl Catal B-Environ* **2015,** *174*, 403-412.
35. Elam, J. W.; Groner, M. D.; George, S. M., Viscous flow reactor with quartz crystal microbalance for thin film growth by atomic layer deposition. *Rev Sci Instrum* **2002,** *73* (8), 2981-2987.
36. Groner, M.; Fabreguette, F.; Elam, J.; George, S., Low-temperature Al2O3 atomic layer deposition. *Chem Mater* **2004,** *16* (4), 639-645.
37. Plakhova, T. V.; Romanchuk, A. Y.; Butorin, S. M.; Konyukhova, A. D.; Egorov, A. V.; Shiryaev, A. A.; Baranchikov, A. E.; Dorovatovskii, P. V.; Huthwelker, T.; Gerber, E., Towards the surface hydroxyl species in CeO 2 nanoparticles. *Nanoscale* **2019,** *11* (39), 18142-18149.
38. Mullins, D. R.; Albrecht, P. M.; Chen, T. L.; Calaza, F. C.; Biegalski, M. D.; Christen, H. M.; Overbury, S. H., Water Dissociation on CeO2(100) and CeO2(111) Thin Films. *J Phys Chem C* **2012,** *116* (36), 19419-19428.
39. Beche, E.; Charvin, P.; Perarnau, D.; Abanades, S.; Flamant, G., Ce 3d XPS investigation of cerium oxides and mixed cerium oxide (CexTiyOz). *Surf Interface Anal* **2008,** *40* (3-4), 264-267.
40. Burroughs, P.; Hamnett, A.; Orchard, A. F.; Thornton, G., Satellite Structure in X-Ray Photoelectron-Spectra of Some Binary and Mixed Oxides of Lanthanum and Cerium. *J Chem Soc Dalton* **1976,** (17), 1686-1698.

41. Praline, G.; Koel, B. E.; Hance, R. L.; Lee, H. I.; White, J. M., X-Ray Photoelectron Study of the Reaction of Oxygen with Cerium. *J Electron Spectrosc* **1980,** *21* (1), 17-30.
42. Paparazzo, E.; Ingo, G. M.; Zacchetti, N., X-Ray-Induced Reduction Effects at Ceo2 Surfaces - an X-Ray Photoelectron-Spectroscopy Study. *J Vac Sci Technol A* **1991,** *9* (3), 1416-1420.
43. Romeo, M.; Bak, K.; Elfallah, J.; Lenormand, F.; Hilaire, L., Xps Study of the Reduction of Cerium Dioxide. *Surf Interface Anal* **1993,** *20* (6), 508-512.
44. Mullins, D. R.; Overbury, S. H.; Huntley, D. R., Electron spectroscopy of single crystal and polycrystalline cerium oxide surfaces. *Surf Sci* **1998,** *409* (2), 307-319.
45. Kotani, A.; Jo, T.; Parlebas, J. C., Many-Body Effects in Core-Level Spectroscopy of Rare-Earth Compounds. *Adv Phys* **1988,** *37* (1), 37-85.
46. Wang, R. G.; Dangerfield, R., Seed-mediated synthesis of shape-controlled CeO2 nanocrystals. *Rsc Adv* **2014,** *4* (7), 3615-3620.
47. Xu, C.; Qu, X., Cerium oxide nanoparticle: a remarkably versatile rare earth nanomaterial for biological applications. *NPG Asia Materials* **2014,** *6* (3), e90-e90.
48. Dutta, G.; Waghmare, U. V.; Baidya, T.; Hegde, M. S.; Priolkar, K. R.; Sarode, P. R., Reducibility of Ce1-xZrxO2: origin of enhanced oxygen storage capacity. *Catal Lett* **2006,** *108* (3-4), 165-172.
49. Hegde, M. S.; Beraba, P., Noble metal ion substituted CeO2 catalysts: Electronic interaction between noble metal ions and CeO2 lattice. *Catal Today* **2015,** *253*, 40-50.
50. Elam, J. W.; Routkevitch, D.; Mardilovich, P. P.; George, S. M., Conformal coating on ultrahigh-aspect-ratio nanopores of anodic alumina by atomic layer deposition. *Chem Mater* **2003,** *15* (18), 3507-3517.
51. Reinhardt, K.; Winkler, H., Cerium mischmetal, cerium alloys, and cerium compounds. *Ullmann's encyclopedia of industrial chemistry* **2000**.
52. Jiang, L. Q.; Guo, J. K.; Liu, H. B.; Zhu, M.; Zhou, X.; Wu, P.; Li, C. H., Prediction of lattice constant in cubic perovskites. *J Phys Chem Solids* **2006,** *67* (7), 1531-1536.
53. Wang, C.; Wen, C.; Lauterbach, J.; Sasmaz, E., Superior oxygen transfer ability of Pd/MnOx-CeO2 for enhanced low temperature CO oxidation activity. *Appl Catal B-Environ* **2017,** *206*, 1-8.
54. Hou, X. L.; Lu, Q. Q.; Wang, X. C., Enhanced catalytic properties of La-doped CeO2 nanopowders synthesized by hydrolyzing and oxidizing Ce46La5C49 alloys. *J Sci* **2017,** *2* (1), 41-44.
55. Gupta, A.; Hegde, M. S.; Priolkar, K. R.; Waghmare, U. V.; Sarode, P. R.; Emura, S., Structural Investigation of Activated Lattice Oxygen in Ce1-xSnxO2 and Ce1-x-ySnxPdyO2-delta by EXAFS and DFT calculation. *Chem Mater* **2009,** *21* (24), 5836-5847.
56. Gupta, A.; Kumar, A.; Waghmare, U. V.; Hegde, M. S., Origin of activation of Lattice Oxygen and Synergistic Interaction in Bimetal-Ionic Ce0.89Fe0.1Pd0.01O2-delta Catalyst. *Chem Mater* **2009,** *21* (20), 4880-4891.
57. Scanlon, D. O.; Morgan, B. J.; Watson, G. W., The origin of the enhanced oxygen storage capacity of Ce1-x(Pd/Pt)(x)O-2. *Phys Chem Chem Phys* **2011,** *13* (10), 4279-4284.
58. Shapovalov, V.; Metiu, H., Catalysis by doped oxides: CO oxidation by AuxCe1-xO2. *J Catal* **2007,** *245* (1), 205-214.
59. Yang, Z. X.; Luo, G. X.; Lu, Z. S.; Woo, T. K.; Hermansson, K., Structural and electronic properties of NM-doped ceria (NM = Pt, Rh): a first-principles study. *J Phys-Condens Mat* **2008,** *20* (3).

Figures

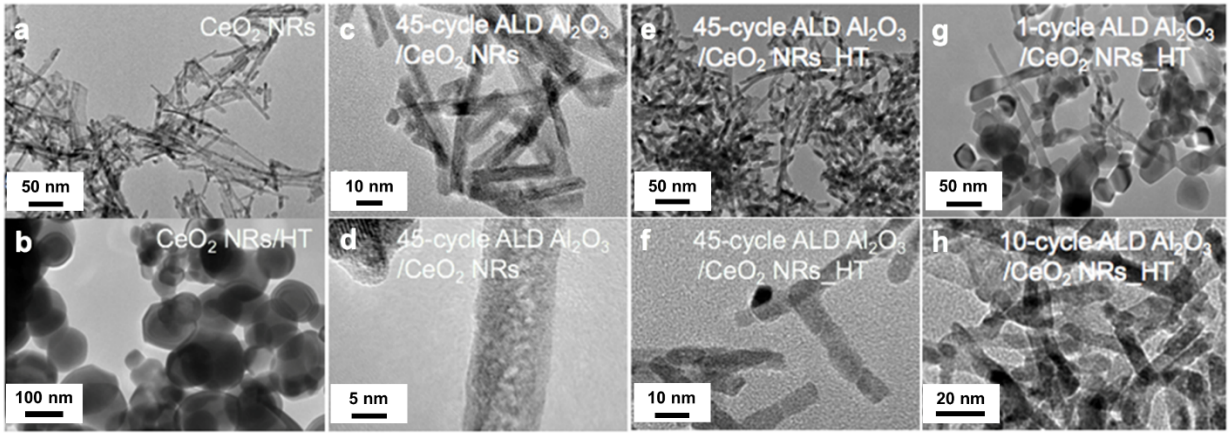

Figure 1. TEM images of **(a)** CeO_2 NRs; **(b)** CeO_2NRs_HT (CeO_2 NRs after HT); **(c, d)** CeO_2 NRs/45Al_2O_3; **(e, f)** CeO_2 NRs/45Al_2O_3_HT;**(g)** CeO_2 NRs/1Al_2O_3_HT; **(h)** CeO_2 NRs/45Al_2O_3. CeO_2 NRs/nAl_2O_3_HT: CeO_2 NRs with n cycles of Al_2O_3 ALD coating followed by HT. HT: heat treatment at 700 ºC in N_2 for 5 h. ALD Al_2O_3 is carried at 200 ºC with trimethyl aluminum [$Al(CH_3)_3$] & H_2O as the reactants.

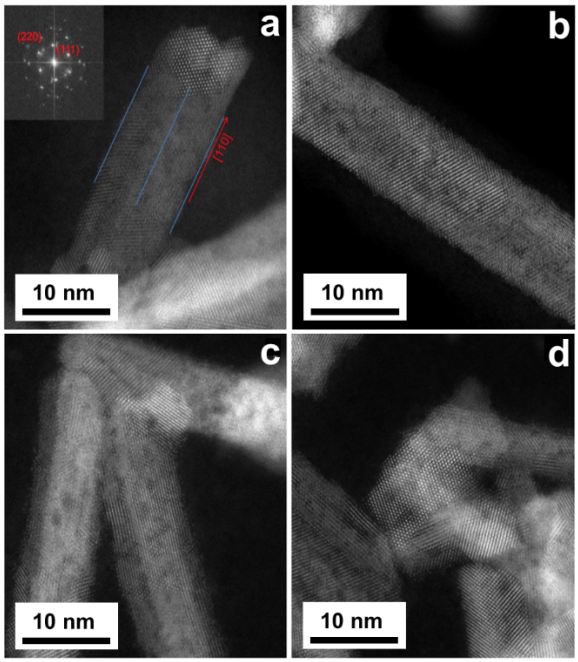

Figure 2. HRTEM of fresh CeO_2 NRs (**a** and **b**) and CeO_2NRs/45Al_2O_3 (**c** and **d**) before the thermal treatment. The inset figure in (a) shows the corresponding Fourier transform image of the CeO_2 NR. The arrow in (a) illustrates the [110] direction of CeO_2 NRs.

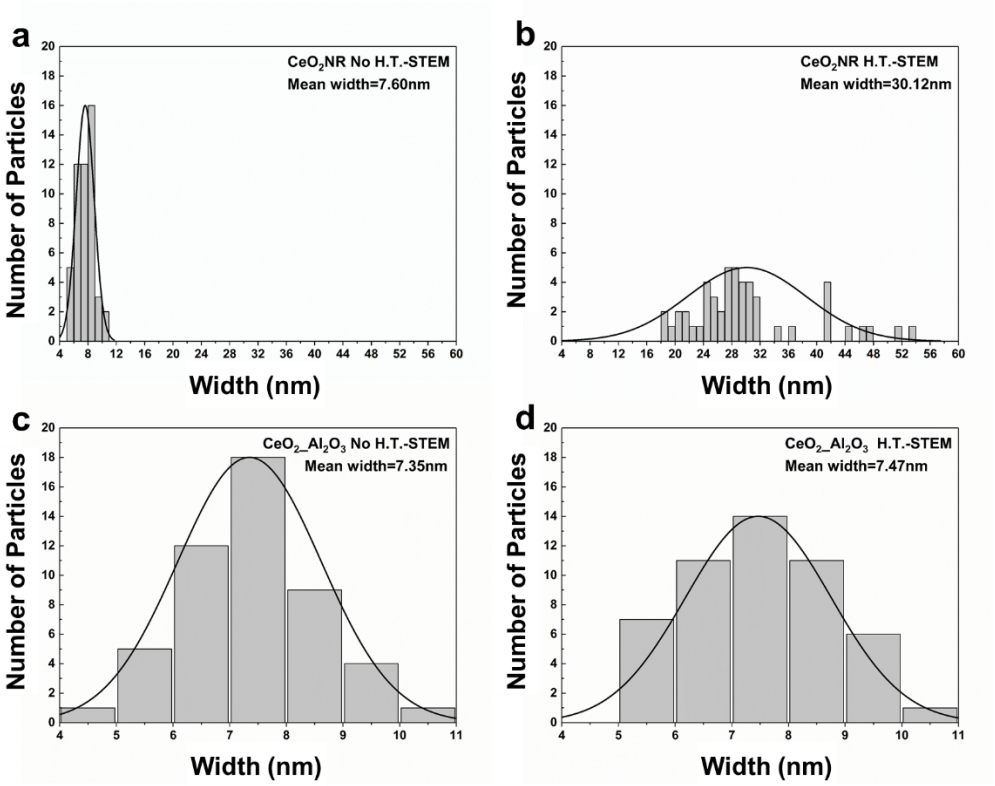

Figure 3. CeO_2 nanoparticle size distribution of (a) Non-treated CeO_2 NRs; (b) Non-treated CeO_2 NRs after HT; (c) 45-c ALD treated CeO_2 NRs; (d) 45-c ALD treated CeO_2 NRs after HT. Average size of the non-treated CeO_2 nanoparticles increased significantly after HT but remain the same after ALD treatment and HT after ALD treatment. Morphology of the CeO_2 NRs stabilized at least at 700˚C.

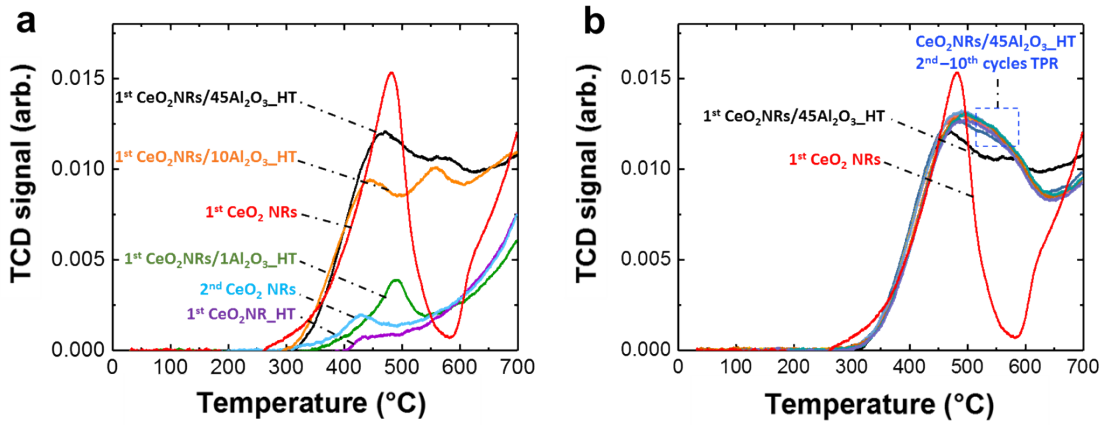

Figure 4. H_2 TPR profile of **(a)** Non-treated CeO_2 NRs in 1st – 2nd cycles of TPR; non-treated CeO_2 NRs after HT; 1, 10, 45 cycles ALD treated CeO_2 NRs after HT for comparison; **(b)** Non-treated CeO_2 NRs 1st cycle TPR; $45Al_2O_3/CeO_2NR\_HT$ in the 1st – 10th cycles of TPR for recyclable high temperature reaction. The amount of H_2 uptake is normalized to the weight of the sample. The area underneath a curve is a measure of OSC of samples. The ALD Al_2O_3 treated samples should have larger peaks than that in the figure if we use the CeO_2 as the mass base. The low temperature peak at ~ 480 ºC is from surface oxygen. The reduction of bulk oxygen from CeO_2 NRs has a peak located at > 700 ºC. The temperature ramping rate in TPR is 10 ºC/min.

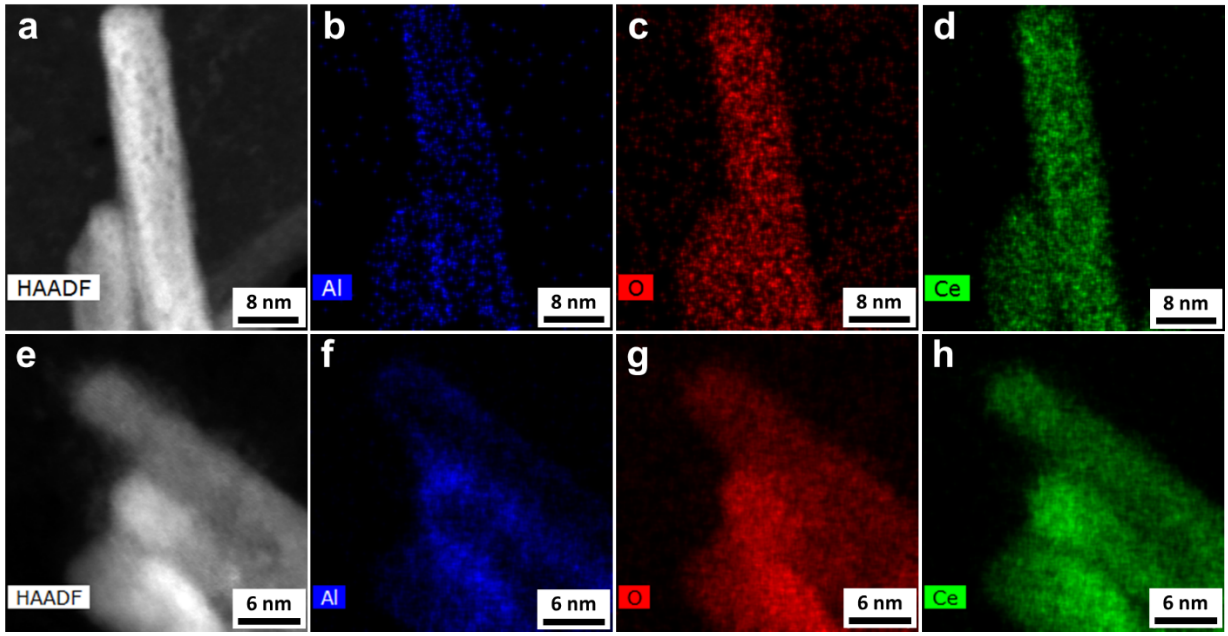

Figure 5. HAADF-STEM EDAX mapping of two selected CeO_2NRs/45Al_2O_3 samples, (a-b) sample 1 and (e-h) sample 2. Morphology is shown in (a and e). Ce (d and h) and O (c and g) are everywhere inside the nanorods. Al (b-f) is only on the surface of the nanorods.

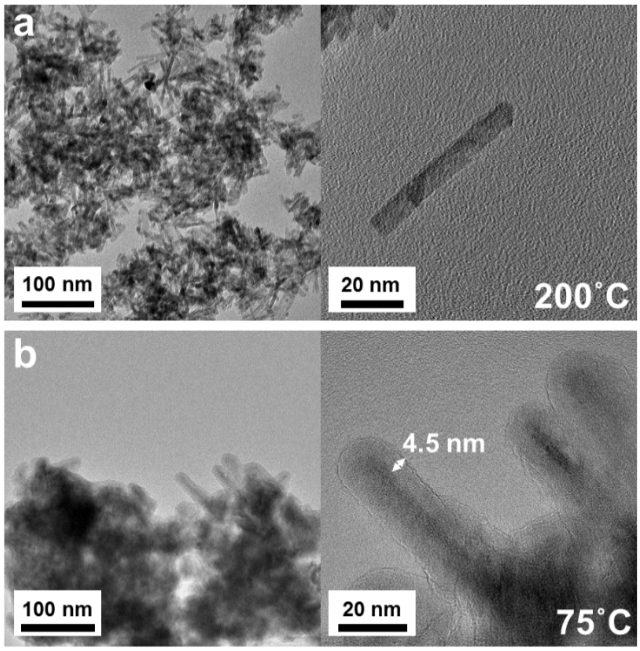

Figure 6. TEM morphology images of CeO_2NR/45Al_2O_3 generated at (a) 200 ˚C and (b) at 75 ˚C via the same ALD Al_2O_3 sequence. No shell can be seen on the sample generated at 200 ˚C. An Al_2O_3 shell with thickness ~4.5 nm can be clearly seen on the sample generated at 75˚C.

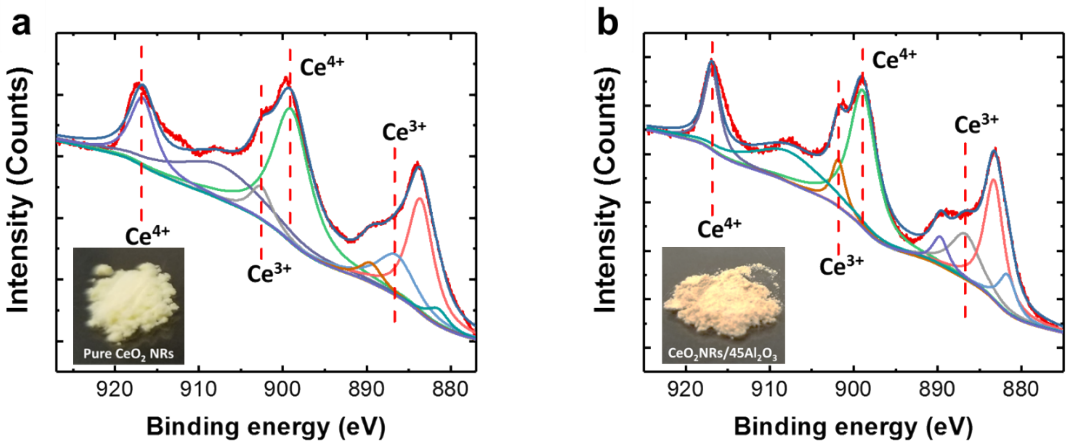

Figure 7. XPS spectra of (a) CeO_2NRs and (b) CeO_2NRs/45Al_2O_3. The concentration of Ce^{3+} increased after 45 Al_2O_3 ALD cycles at 200 ˚C. CeO_2 has been reduced, more O_2 vacancies created. The inset images show the color of the corresponding samples.

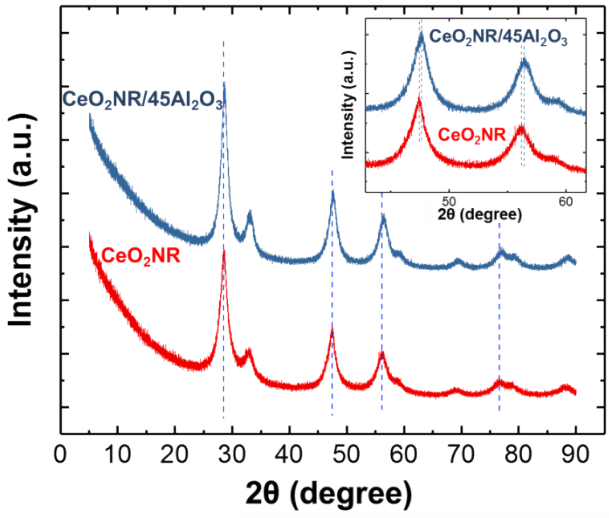

Figure 8. XRD spectra of CeO_2 NRs (bottom) and CeO_2NRs/45Al_2O_3 (top). XRD peaks shifted to higher 2Θ after 45 cycles Al_2O_3 ALD at 200 ˚C, suggesting that the lattice constant of CeO_2NRs/45Al_2O_3 is smaller than that of CeO_2 NRs.

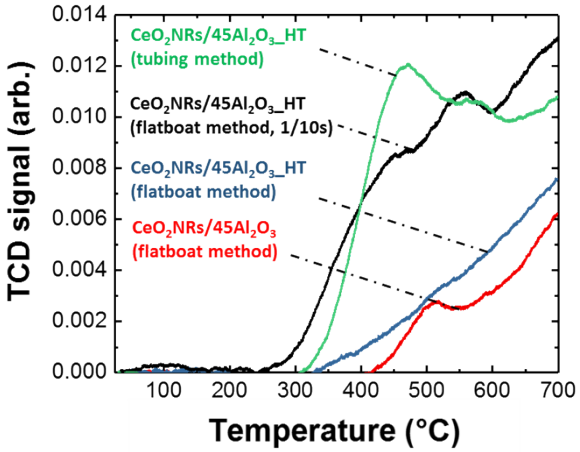

Figure 9. H_2 TPR of CeO_2NR/45Al_2O_3 by tubing method (300 s TMA exposure and 20 s water dose) after HT, CeO_2NR/45Al_2O_3 by flatboat method before and after HT, CeO_2NR/45Al_2O_3 by flatboat method with 1/10 TMA and water exposure time (30s TMA exposure and 2s water dose) after HT. The temperature ramping rate in TPR is 10 ºC/min.

Supplemental Information

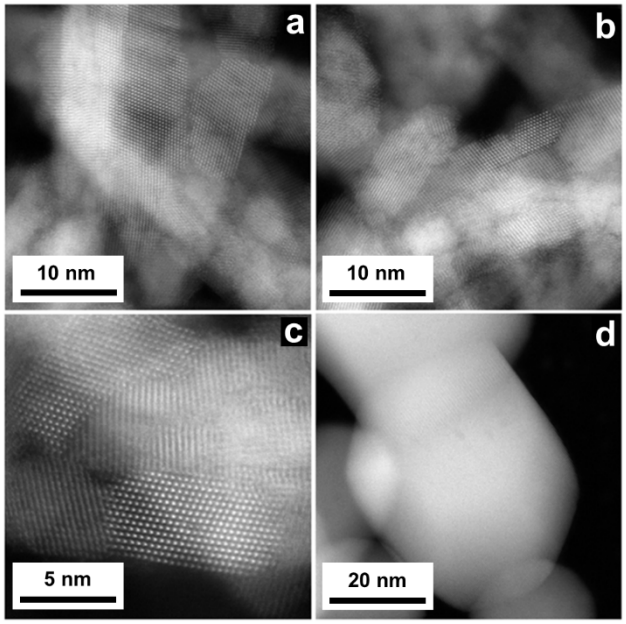

Figure S1. STEM images of (a-c) /CeO_2NRs/45Al_2O_3_HT and (d) CeO_2NRs_HT.

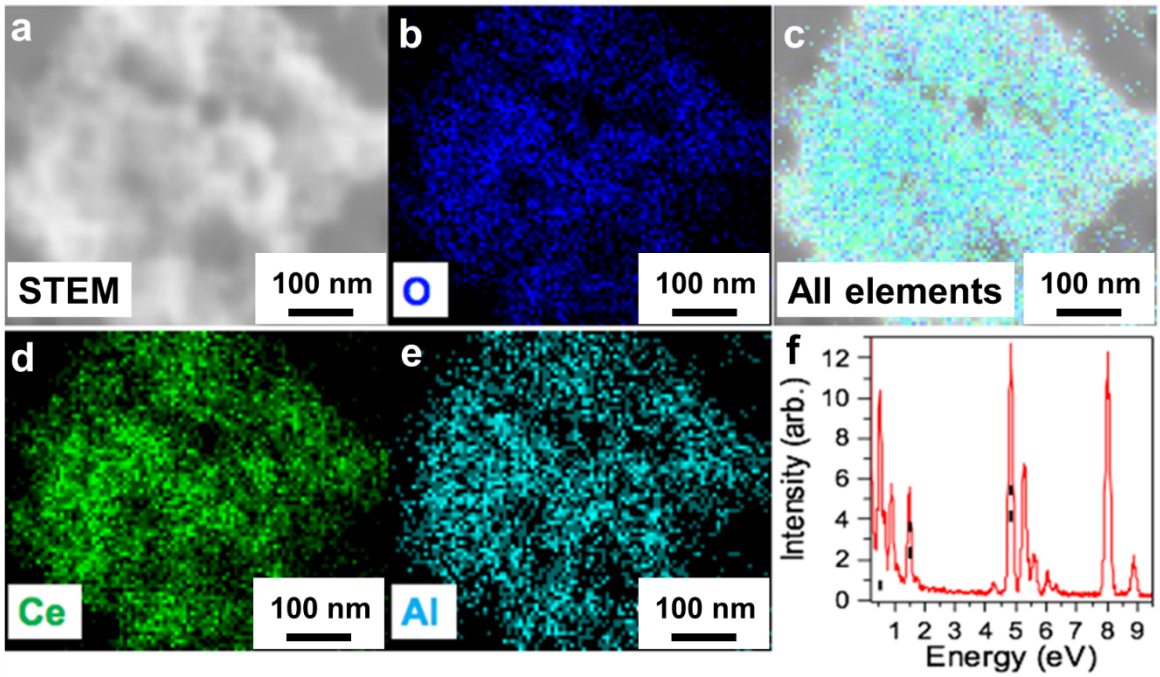

Figure S2. STEM EDAX mapping of overall CeO_2NRs/45Al_2O_3 sample. Both the imaging data and the spectrum shows the Al is evenly distributed on the nanorods.